

CHIANTI – an atomic database for emission lines - Paper XVI: Version 10, further extensions

G. DEL ZANNA,¹ K. P. DERE,² P. R. YOUNG,^{3,4} AND E. LANDI⁵

¹*DAMTP, Center for Mathematical Sciences, University of Cambridge, Wilberforce Road, Cambridge, CB3 0WA, UK*

²*College of Science, George Mason University, 4400 University Drive, Fairfax, VA 22030, USA*

³*NASA Goddard Space Flight Center, Code 671, Greenbelt, MD 20771, USA*

⁴*Northumbria University, Newcastle Upon Tyne NE1 8ST, UK*

⁵*Department of Climate, Space Sciences and Engineering, University of Michigan, Ann Arbor, MI, 48109*

Submitted to ApJ

ABSTRACT

We present version 10 of the CHIANTI package. In this release, we provide updated atomic models for several helium-like ions and for all the ions of the beryllium, carbon and magnesium isoelectronic sequences that are abundant in astrophysical plasmas. We include rates from large-scale atomic structure and scattering calculations that are in many cases a significant improvement over the previous version, especially for the Be-like sequence, which has useful line diagnostics to measure the electron density and temperature. We have also added new ions and updated several of them with new atomic rates and line identifications. Also, we have added several improvements to the IDL software, to speed up the calculations and to estimate the suppression of dielectronic recombination.

Keywords: atomic processes — atomic data — Sun: UV radiation — Sun: X-rays, gamma rays — Ultraviolet: general – line synthesis

1. INTRODUCTION

CHIANTI¹ is an atomic database and associated codes for the analysis of optically-thin line and continuum plasma emission. Version 9 (Dere et al. 2019a) of the CHIANTI database provided significant improvements for the X-Ray satellite lines, with new atomic data and a new method for the calculation of the line emissivities that took into account density-dependent effects (due to the metastability of levels in the recombining ions). Several ions were included in the new modeling.

In this version we significantly extend the database. We extend the calculations of the satellite lines to new ions, improve atomic rates for three isoelectronic sequences and add to the database several new minor ions (those not astrophysically abundant). We also correct a few spectral line misidentifications.

We use various sources of atomic data, but for the important collisional excitation rates (CE) by electron impact we

mostly rely on large-scale calculations produced by the UK APAP network² (see, e.g. Badnell et al. 2016). Such calculations use the advanced *R*-matrix suite of codes but also provide energy levels and radiative data. Atomic data for the Be-like, Mg-like and C-like have recently been calculated and are included here. These CE rates replace for several ions approximate rates previously calculated with the distorted-wave (DW) method. As the focus of such calculations are the CE rates, the radiative rates for the lowest configurations are often not as accurate as those obtained with other codes. We have therefore included for several ions A-values for the lower configurations from mainly two sets of codes. The first set is maintained by the COMPAS group (see, e.g. Jönsson et al. 2017) and consists of codes for Multiconfiguration Dirac-Hartree-Fock (MCDHF) calculations, providing very accurate transition probabilities (typically uncertainties are estimated to be within a few percent). The MCDHF calculations have been using the various improvements (e.g. GRASP2K, see Jönsson et al. 2007; Jönsson et al. 2013) of Ian Grant’s relativistic atomic structure program GRASP (Grant et al. 1980; Dyall et al. 1989). The second set are

Corresponding author: G. Del Zanna
 gd232@cam.ac.uk

¹ www.chiantidatabase.org

² apap-network.org

the Multiconfiguration Hartree-Fock (MCHF) calculations, available at NIST³ (see, e.g. [Froese Fischer et al. 2016](#), for a recent description of the methods).

Experimental energies are generally taken from the NIST⁴ compilation, although in several cases, detailed in the comments of each file, alternative or additional identifications have been adopted. As the GRASP2K MCDHF calculations provide very accurate wavelengths (typically within a fraction of an Å), in several cases they have helped to track questionable or incorrect identifications present in NIST or in CHIANTI.

The atomic data for the Be- and Mg-like sequences were benchmarked by [Del Zanna \(2019\)](#) against medium-resolution quiet-Sun irradiances from 60 to 1100 Å measured in 2008 by the prototype Extreme Ultraviolet Variability Experiment (EVE) on the Solar Dynamics Observatory (SDO) ([Woods et al. 2012](#)). The comparison indicated that, at least for medium-resolution spectral data, the CHIANTI data are now relatively complete in the extreme ultraviolet. Good overall agreement between predicted and observed irradiances was found, at a level comparable to the accuracy of the radiometric calibration (10-30%).

2. NEW ATOMIC DATA FOR IONS IN THE HELIUM ISOELECTRONIC SEQUENCE

The ions in the helium isoelectronic sequence produce some of the most intense lines in the X-ray spectrum. In addition, as pointed out by [Gabriel & Jordan \(1969\)](#), selected ratios of the spectral lines provide temperature and density sensitive diagnostics that are often used in the analysis of astrophysical spectra. The helium-like ions also produce satellite lines to the hydrogen-like emission lines. While these are weaker than the satellite lines produced by the lithium-like ions, they have been observed in solar flares ([Parmar et al. 1981; Tanaka et al. 1982; Pike et al. 1996](#)) and in laboratory spectra ([Rice et al. 2014; Weller et al. 2019](#)).

The $1s2s\ ^3S_1$ and $1s2p\ ^1P_1, ^3P_2$ and 3P_1 levels give rise to strong transitions to the ground level $1s^2\ ^1S_0$ that are labeled as z, w, x and y in standard notation ([Gabriel 1972](#)). The temperature sensitive ratio, G , is given as $(x+y+z)/w$ and the density sensitive ratio, R is given by $z/(x+y)$. In the case of Ne IX, [Smith et al. \(2009\)](#) has shown that these ratios are influenced by radiative and dielectronic recombination. The Version 8 release of the CHIANTI database included radiative recombination into the helium-like levels through $1s8l$. In this release, the effects of dielectronic recombination are reproduced by including the configurations above the ionization potential, $2snl$ ($n=2-8, l=0-7$) and $2pnl$ ($n=2-8, l=1-7$).

In this release, we provide updated atomic models for the helium-like ions of C, N, O, Ne, Mg, Al, Si, S, Ar, Ca, Fe, Ni, and Zn and new atomic models for Ti and Cr.

2.1. Energy levels

The energy level files in CHIANTI contain values based on both observations and theoretical calculations. The theoretical energy levels have either been taken from the literature or calculated with the AUTOSTRUCTURE program ([Badnell 2011](#)). In the past, we have relied heavily on observed energy levels provided by [Kramida et al. \(2015\)](#). Currently, the NIST database contains energy levels based on observed spectra for the helium-like ions of C, N, O, and Ne. These energies appear to come from a publication by [Kelly \(1987\)](#) and we have used these for this release. NIST energy levels for other members of the helium isoelectronic sequence are theoretical. The release of version 3 of the CHIANTI database ([Dere et al. 2001](#)) contained observed energy levels from version 1 of the NIST database ([Martin & Dalton 1995](#)). The energies in the current version of NIST ([Kramida et al. 2015](#)) appear to be unchanged since then. These energies have been used to create the new CHIANTI ions Ti XXI and Cr XXIII.

Because of the lack of updated energies in the NIST database, we have taken the approach of relying heavily on the calculations with AUTOSTRUCTURE. As with our work on the lithium isoelectronic sequence ([Dere et al. 2019b](#)), we have used the available energies derived from measured wavelengths to tune the AUTOSTRUCTURE calculations by means of a SHIFTIC file. For levels above the ionization potential, the same has been done but with the theoretical energies of [Goryaev et al. \(2017\)](#) for the $2l2l'$ and $2l3l'$ levels and the theoretical energies of Safranova as reported in [Kato et al. \(1997\)](#).

Recently, [Chantler et al. \(2014\)](#) has suggested that there is a divergence between the theoretical energy levels and the measured energy levels for the w, x, y and z lines. They find this discrepancy begins at around a Z of 20. [Indelicato \(2019\)](#) has compared several calculations of the helium-like energies of the $n=2$ configuration with measurements available in the literature. He finds a discrepancy between experiment and theory that follows a Z^4 behaviour and becomes apparent around $Z \sim 20$. However [Malyshev et al. \(2019\)](#) have performed *ab initio* QED calculations and have found no discrepancy with the modern measurements.

Given the lack of availability of measurement in the NIST database and the potential discrepancy between experiment and theory, we have conducted a modest search for observed wavelengths for the w, x, y and z lines. Wavelengths for the w line are most commonly found and the x line found on occasion.

2.1.1. Observed energy levels for S XV

³ <https://nle.nist.gov/MCHF/periodic.html>

⁴ https://physics.nist.gov/PhysRefData/ASD/levels_form.html

Very accurate measurements of the $1s2p\ ^1P_1$ energy are provided by [Kubiček et al. \(2014\)](#) and [Schleinkofer et al. \(1982\)](#) provide measurements of transition energies for the $1s2p\ ^3P_1$ energy.

2.1.2. Observed energy levels for Ar XVII

[Machado et al. \(2018\)](#) has made accurate measurements of the Ar XVII w line using an electron cyclotron ion source (ECRIS). These are used to provide the observed energy of the $1s2p\ ^1P_1$ level.

2.1.3. Observed energy levels for Ca XIX

[Rice et al. \(2014\)](#) performed high resolution measurements of the Ca XIX w , x , y , and z lines of plasmas created at the ALCATOR MOD-Z tokamak and these measurements have been used in the current database.

2.1.4. Observed energy levels for Ti XXI

[Payne et al. \(2014\)](#) used an EBIT source to perform accurate measures of the wavelengths of the w , x , y and z lines of Ti XXI and these have been inserted into the current database.

2.1.5. Observed energy levels for Cr XXIII

[Beiersdorfer et al. \(1989\)](#) have measured the wavelengths of several lines of Cr XXIII with the Princeton Large Torus tokamak. These measurements correspond to the decay of the $1s2p\ ^1P_1$, $1s4p\ ^1P_1$ and $1s5p\ ^1P_1$ levels to the $1s^2\ ^1S_0$ ground level. Their experimental precision is stated to be $\Delta\lambda/\lambda$ of 1/20000.

2.1.6. Observed energy levels for Fe XXV

Very accurate measurements of the $1s2p\ ^3P_1$ and the $1s2p\ ^1P_1$ levels are provided by [Rudolph et al. \(2013\)](#). These measurements are based on synchrotron illumination of highly Fe ions in an electron beam ion trap (EBIT) with the synchrotron beam finally detected with a crystal monochromator. In addition, [Briand et al. \(1984\)](#) provide measurements of the wavelength of the $1s^2\ ^1S_0 - 1s2p\ ^3P_2$ transition. [Beiersdorfer et al. \(1989\)](#) has provided measurements of the same transitions as they provided for Cr XXIII.

2.2. Transition Rates

For the various transition rates, such as A-values and autoionization rates, AUTOSTRUCTURE has been utilized. A comparison of the autoionization rates with those of [Goryaev et al. \(2017\)](#) and [Kato et al. \(1997\)](#) shows good agreement for the $n=2$ levels, moderate agreement for the $n=3$ levels and decreasing levels of agreement for the $n=4$ and $n=5$ levels. The two-photon decay rate for the $1s^2\ ^1S_0 - 1s2s\ ^1S_0$ transition is provided by [Derevianko & Johnson \(1997\)](#).

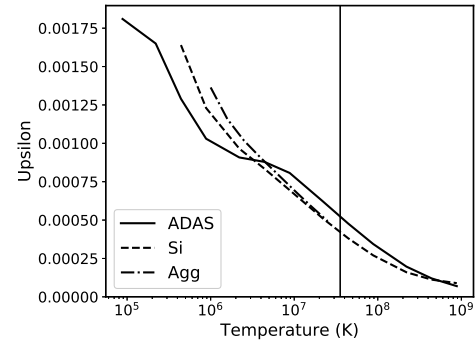


Figure 1. The effective collision strengths Upsilon for the $1s^2\ ^1S_0$ to the $1s2s\ ^3S_1$ transition in Ti XXI. The vertical line is where the contribution function for the reverse transition is a maximum. ADAS refers to [Whiteford et al. \(2001\)](#), Si refers to [Si et al. \(2017\)](#) and Agg refers to [Aggarwal & Keenan \(2012\)](#)

2.3. Effective Collision Strengths

For the pre-existing ions in the helium-like sequence, the effective collision strengths have been taken from the radiation-damped intermediate coupling frame transformation R-matrix calculations of [Whiteford et al. \(2001\)](#). For the ions new to this release, Ti XXI and Cr XXIII, there are two other sets of calculations that are available, those of [Aggarwal & Keenan \(2012\)](#) and [Si et al. \(2017\)](#). It is worthwhile to compare these effective collision strengths with those of [Whiteford et al. \(2001\)](#) for the transitions from the ground level to the $1s2s$ and $1s2p$ levels for Ti XXI. The calculations of [Si et al. \(2017\)](#) tend to agree quite well with those of [Aggarwal & Keenan \(2012\)](#) at about the 10% level or better at the temperature where the calculations overlap. However, the collision strengths of [Aggarwal & Keenan \(2012\)](#) do not extend to temperatures where the contribution functions for these transition maximizes (T_{max}). The most realistic comparison then is between the values of Si and those of Whiteford. [Si et al. \(2017\)](#) employed the independent process and isolated resonances approximation using distorted waves. The calculations were made with the Flexible Atomic Code (FAC; [Gu 2008](#)). In Fig. 1 a comparison of the three calculations for the $1s^2\ ^1S_0 - 1s2s\ ^3S_1$ collision strength is shown. This is largely responsible for producing the z line. At T_{max} the Whiteford values are about 20% higher than those of Si. For most transitions to the $1s2s$ and $1s2p$ levels, the values of Whiteford and Si show an agreement at about the 10% level.

For the present release, the calculations of Whiteford et al. for the ions along the sequence have been used (and re-fitted), as made available on the UK APAP and OPEN-ADAS web sites.

2.4. Diagnostic ratios involving the Fe XXV satellites

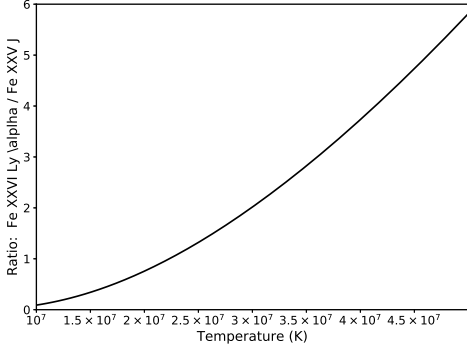


Figure 2. The ratio of the Fe XXVI Ly α lines to the Fe XXV J satellites.

As noted, the helium-like J satellites to the hydrogen-like Ly α lines have been observed and the ratio of the two provide a temperature diagnostic for high temperature plasmas. The J satellites are a collection of lines at somewhat longer wavelengths than the Ly α lines. [Parmar et al. \(1981\)](#) used the calculations of [Dubau et al. \(1981\)](#) for the analysis of their data. More recently, the observations of [Pike et al. \(1996\)](#) were analyzed with the updated calculations of [Dubau et al. \(1981\)](#). The new atomic data in CHIANTI allows one to calculate this ratio and the ratio is shown in Fig. 2. The ratio is comparable to that shown in [Pike et al. \(1996\)](#).

3. NEW ATOMIC DATA FOR THE BERYLLIUM ISOELECTRONIC SEQUENCE

It is well-known (cf. the review by [Del Zanna & Mason 2018](#)) that spectral lines from Be-like ions are prominent and provide important density and temperature diagnostics. Of all the isoelectronic sequences, this was the one where the CHIANTI atomic data needed improvements. In fact, for several Be-like ions, previous CHIANTI versions had either interpolated collisional rates ([Keenan et al. 1986](#)), or had sufficiently accurate data only for the $n = 2$ (and sometimes $n = 3$) levels. As previously shown in [Del Zanna et al. \(2008\)](#) for an important ion for the solar corona, Mg IX, interpolation of the rates can lead to incorrect results such as temperatures (with differences up to 50%).

As a baseline, we have adopted the CE rates calculated by [Fernández-Menchero et al. \(2014a\)](#) (from B II Zn XXVII) within the UK APAP network with the Breit-Pauli R -matrix suite of codes and the ICFT method. The CI and CC expansions included atomic states up to $nl = 7d$, for a total of 238 fine-structure levels. Good agreement with the previous R -matrix CE rates for Mg IX ([Del Zanna et al. 2008](#)) and Fe XXIII ([Chidichimo et al. 2005](#)) were found by [Fernández-Menchero et al. \(2014a\)](#), but significant differences with other calculations are present. The $n = 6, 7$ levels only included $l = s, p, d$ states, which were added to improve the rates for the lower levels. We have retained only the main

configurations up to $n = 5$, as the rates (both A-values and collisional ones) for the $n = 6, 7$ levels are not reliable (see the discussion in [Del Zanna et al. 2020](#)).

For some ions, the levels above the ionization threshold have not been included, as proper treatment would require an extended two-ion model, including autoionisation rates. Only transition probabilities with a branching ratio greater than 10^{-5} have been retained.

For the radiative data, we have replaced the values for the lowest configurations with data that are generally more accurate, checking that deviations for the strongest transitions were within 10–30%. We mainly used the MCHF calculations by [Tachiev & Froese Fischer \(1999\)](#) and those of [Wang et al. \(2015\)](#) for the ions with $Z=10–30$. The latter used a combined Configuration Interaction and Many-body Perturbation Theory Approach (MBPT). Duplicates in the MCHF data were removed, and multipolar transition probabilities added.

Comparisons with the earlier datasets show significant changes (20–30%) in the line intensities for many ions, even for the strong transitions. Experimental energies are taken from the NIST database, except where noted below.

3.1. C III

As a baseline we adopted the atomic data of [Fernández-Menchero et al. \(2014a\)](#). Only the lowest 75 bound levels up to $n = 5$ were retained. For the lowest 20 levels we adopted the A-values from the MCHF calculations by [Tachiev & Froese Fischer \(1999\)](#). Experimental energies are taken from NIST. Significant differences are present in the density- and temperature-sensitive ratio of the $2s\ 2p\ ^1P-2p\ ^2P\ 1S\ 1247.4\ \text{\AA}$ line with the lines of the $1176\ \text{\AA}$ multiplet ($2s\ 2p\ ^3P-2p\ ^2P\ ^3P$), when compared to the previous model, which included only the $n = 2, 3$ levels.

3.2. N IV

N IV has been the subject of extensive studies on the collisional rates. [Aggarwal et al. \(2016\)](#) performed relativistic electron scattering calculations for this ion with the DARC code, finding significant discrepancies with the ICFT results of [Fernández-Menchero et al. \(2014a\)](#), questioning the validity of the ICFT method. Previous doubts from the same authors were published ([Aggarwal & Keenan 2015](#)), leading to a discussion on the importance of the target structure description by [Fernández-Menchero et al. \(2015a\)](#).

[Fernández-Menchero et al. \(2017\)](#) performed a large-scale electron impact excitation calculation for N IV using the B-spline R-matrix method, and compared the results with the ICFT and the DARC ones. The paper highlighted the importance of the target structure description and especially the size of the close-coupling expansion, pointing out that collisional rates to highly excited levels can be inaccurate, because of the limitation in the expansion.

The three sets of atomic rates obtained with the different methods provided an opportunity to obtain some estimates on the uncertainties, as well as their effect on the calculated emissivities of the lines. [Del Zanna et al. \(2019\)](#) showed that for astrophysical applications the three sets of data are equivalent, as very small (typically 10%) variations in the emissivities of the stronger lines were found.

For the present model we adopt the results of the B-spline method, as this was the largest-scale calculation, providing much better target energies than the other methods. Only the lowest 136 bound levels have been retained. Experimental energies from NIST as assessed by [Fernández-Menchero et al. \(2017\)](#) have been included.

3.3. O v

O v is another important ion. The previous CHIANTI model was quite large, as it included a full set of configuration up to $n = 5$. However, the collisional rates for most levels were calculated with the distorted wave method, except for the lower levels for which the results of an unpublished *R*-matrix calculation were used.

As a baseline we adopted the atomic data of [Fernández-Menchero et al. \(2014a\)](#). Only the 166 bound levels up to $n=5$ have been retained, reordering the indexing of the original calculation. For the lowest 20 levels we adopted the A-values from the MCHF calculations by [Tachiev & Froese Fischer \(1999\)](#). Experimental energies are taken from NIST. Only a few differences with the values in the previous CHIANTI version are present. However, we caution that several NIST energy values are not relative to the ground state, so the corresponding wavelengths might not be accurate. It is worth noting that the new model provides electron densities from within the lines in the 760 Å multiplet that are about 60% higher than the previous model. These lines have been resolved with e.g. the Solar and Heliospheric Observatory (SoHO) Solar Ultraviolet Measurements of Emitted Radiation (SUMER, see [Wilhelm et al. 1995](#)), and are now observed with the Solar Orbiter Spectral Imaging of the Coronal Environment (SPICE) spectrometer ([Anderson et al. 2019](#)).

3.4. Ne VII

The previous CHIANTI model for Ne VII had 46 $n = 2,3$ levels, and *R*-matrix collisional rates. As in O v, we retained the 166 bound levels up to $n = 5$ of the [Fernández-Menchero et al. \(2014a\)](#) APAP data. Experimental energies are taken from NIST, but as in O v some values are not relative to the ground state so are uncertain. For the $n = 2,3$ (lowest 46 levels) we adopted the A-values from the MBPT calculations of [Wang et al. \(2015\)](#), finding very small differences (10% or so) with the APAP data.

3.5. Na VIII

The previous CHIANTI model for Na VIII had only the 10 lowest $n = 2$ levels, with collisional rates interpolated along the sequence. As in the previous cases, we retained the 166 bound levels up to $n = 5$ of the [Fernández-Menchero et al. \(2014a\)](#) data. The present model is therefore a significant improvement over the previous one. Experimental energies are taken from NIST. For the $n = 2,3$ (lowest 46 levels) we adopted the A-values from the MBPT calculations of [Wang et al. \(2015\)](#).

3.6. Mg IX

Mg IX is an important ion for the solar corona, as it provides excellent temperature diagnostics (available with the Solar Orbiter SPICE spectrometer), see e.g. [Del Zanna et al. \(2008\)](#) and references therein. The previous CHIANTI model ion had 108 levels, with *R*-matrix collisional rates for the lowest 98 up to $n = 4$, and a few $n = 5$ levels with DW rates. As in previous ions, we retained the 166 bound levels up to $n = 5$ of the [Fernández-Menchero et al. \(2014a\)](#) data. The collision rates are close to the previous ones, so minor differences with the previous model are present. Experimental energies are taken from the previous CHIANTI version and from NIST. For the $n = 2,3$ (lowest 46 levels) we adopted the A-values from the MBPT calculations of [Wang et al. \(2015\)](#).

3.7. Al X

The previous CHIANTI model for Al X had only the 10 lowest $n = 2$ levels, with collisional rates interpolated along the sequence, so the new model is a significant improvement. As in previous ions, we retained the 166 bound levels up to $n = 5$ for the [Fernández-Menchero et al. \(2014a\)](#) data. Experimental energies for most levels have been taken from [Khardi et al. \(1994\)](#) as the NIST compilation is not complete. For the $n = 2,3$ (lowest 46 levels) we adopted the A-values from the MBPT calculations of [Wang et al. \(2015\)](#).

3.8. Si XI

The previous model had *R*-matrix collisional rates calculated with a small target, only the 10 lowest $n = 2$ levels, and only at intermediate energies. The rest of the CHIANTI model contained DW collisional rates. The present model has the data for the 166 bound levels up to $n = 5$ from [Fernández-Menchero et al. \(2014a\)](#). For the $n = 2,3$ (lowest 46 levels) we adopted the A-values from the MBPT calculations of [Wang et al. \(2015\)](#).

Experimental energies have been re-assessed as both the previous CHIANTI version and the NIST values are surprisingly not complete. The values recommended by the extensive compilation of [Kramida & Träbert \(1995\)](#) have been adopted. These authors also provided LSJ percentage composition which was key to identify many of the strongly spin-orbit mixed levels, where level assignment becomes difficult.

They also provided uncertainty estimates for the observed energies. Their values are significantly different in many cases from those in NIST and in the previous CHIANTI version, but are generally very close to the theoretical energies of the new model. In a few cases, tentative energies have been assigned as observed, while in a couple of cases the Kramida & Träbert (1995) values could not be assigned to a level.

The new model for Si XI is a significant improvement for this important ion. Long-standing problems between predicted and observed intensities for this ion have been present for solar active regions. The strongest lines were observed by the SoHO CDS instrument. To illustrate the difference with the previous model, we have considered a CDS full-spectral atlas of an active region obtained on 1997 September 25 between 18:01 and 18:56 UT (s9253r00). This observation was one of those considered for the CDS in-flight calibration (Del Zanna 1999; Del Zanna et al. 2001). A spatial area where the Si XI lines were enhanced was selected. The unblended lines were selected and the comparisons between observed and theoretical intensities, as a function of electron density and temperature, are presented in Figures 3,4 in the form of ‘emissivity ratios’ (see Del Zanna et al. 2004; Del Zanna & Mason 2018, for details and examples), which are essentially the ratios of the observed radiances in the lines with their emissivities, as a function of the electron density (or temperature) for a fixed temperature (or density). The ratios are normalised with the same constant for all the lines, so that they are close to unity.

The 371.5 Å line is very weak but is strongly density-dependent. It indicates an electron density about $\times 10^{9.2}$ cm $^{-3}$, with both the previous and current model. This density is typical of active region cores. The 604.1 Å line is also very weak. However, with the present model its intensity agrees with that of the other lines. With the previous version 9 model there is a discrepancy of 50%. The two main lines are the resonance line at 303.3 Å, observed in second order, and the intercombination line at 580.9 Å. They are an excellent temperature diagnostic for active regions (Del Zanna & Mason 2018). With the current model, they indicate $\log T[K]=6.6$, which is a reasonable value for an active region (4 MK). With the previous model, they provide a much lower temperature: $\log T[K]=6.2$, i.e. 1.6 MK.

3.9. P XII

The present model for P XII is also a significant improvement over the previous one, which had only the 10 lowest $n = 2$ levels, with collisional rates interpolated along the sequence. We retained the 166 bound levels up to $n = 5$ of the Fernández-Menchero et al. (2014a) data. Experimental energies are taken from NIST. For the $n = 2, 3$ (lowest 46 lev-

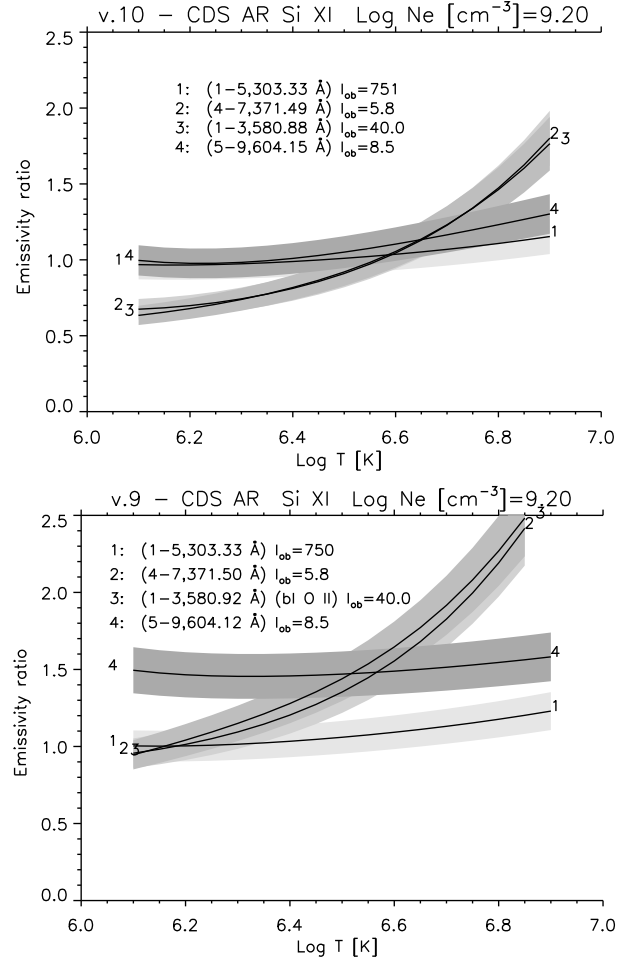


Figure 3. Emissivity ratios of the main Si XI lines observed by SoHO CDS in an active region, with the present v.10 model (above) and the previous one (v.9, below), as a function of temperature. I_{ob} indicates the observed radiances in photon units. The shaded areas indicate the approximate uncertainty in the radiometric calibration.

els) we adopted the A-values from the MBPT calculations of Wang et al. (2015).

3.10. S XIII

S XIII is an important ion to measure the sulfur abundance in solar active regions. The previous model ion had many levels (92), but CE rates for the $n = 2$ levels were interpolated along the sequence, and the other ones were calculated with the DW approach. We retained the 166 bound levels up to $n = 5$ of the Fernández-Menchero et al. (2014a) data. Experimental energies are taken from NIST for the lowest levels, but for the rest energies have been re-assessed, mostly taking the values recommended by Fawcett & Hayes (1987). For the $n = 2, 3$ (lowest 46 levels) we adopted the A-values from the MBPT calculations of Wang et al. (2015).

3.11. Cl XIV

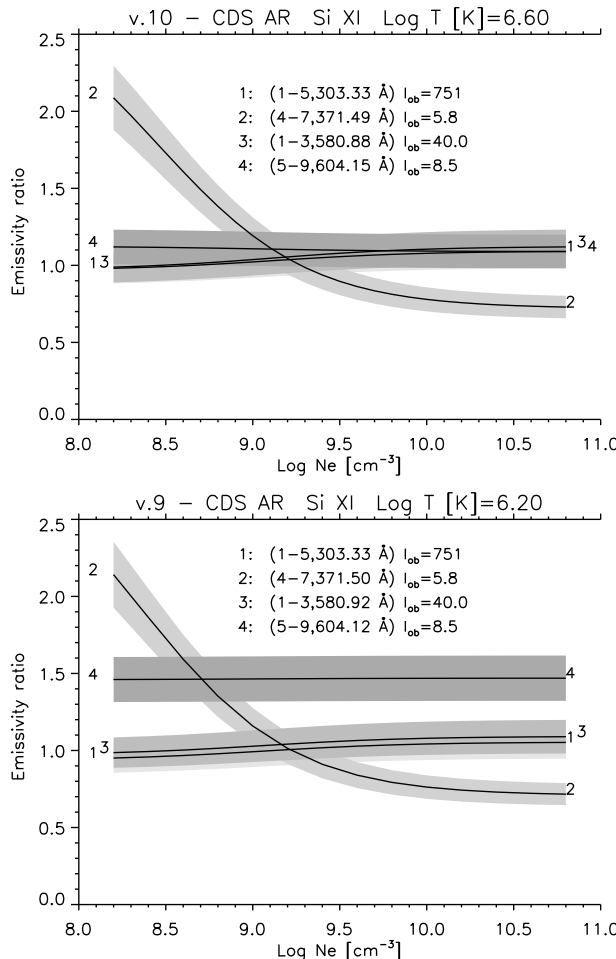


Figure 4. Emissivity ratios of the same lines as in Fig. 3, as a function of the electron density, with the present model (v10, above), and the previous one (v.9, below).

The present model for Cl XIV is a significant improvement over the previous one, which only had the 10 lowest $n = 2$ levels, and CE rates interpolated along the sequence. We retained the 166 bound levels up to $n = 5$ of the Fernández-Mencher et al. (2014a) data. Experimental energies are taken from NIST. For the $n = 2, 3$ (lowest 46 levels) we adopted the A-values from the MBPT calculations of Wang et al. (2015).

3.12. Ar XV

The previous model ion was extended (92 levels), but CE rates for the $n = 2$ states were interpolated along the sequence, and the other ones were calculated with the DW approach. We retained the 166 bound levels up to $n = 5$ of the Fernández-Mencher et al. (2014a) data. Experimental energies are taken from NIST, but we note that many of the $n = 3$ values were actually estimated with quantum defects by Khardi et al. (1994), so the wavelengths of the decays to the lower levels are not necessarily accurate. For the $n = 2, 3$

(lowest 46 levels) we adopted the A-values from the MBPT calculations of Wang et al. (2015).

3.13. K XVI

The present model for K XVI is a significant improvement over the previous one, which only had the 10 lowest $n = 2$ levels, and CE rates interpolated along the sequence. We retained the 166 bound levels up to $n = 5$ of the Fernández-Mencher et al. (2014a) data. Experimental energies are taken from NIST. For the $n = 2, 3$ (lowest 46 levels) we adopted the A-values from the MBPT calculations of Wang et al. (2015).

3.14. Ca XVII

The previous model ion for Ca XVII was relatively accurate, given the importance of this ion. It had 92 levels, with CE rates for the $n = 2$ levels calculated with the *R*-matrix codes, and DW data for the rest of transitions. We retained the 166 bound levels up to $n = 5$ of the Fernández-Mencher et al. (2014a) data. Experimental energies are taken from the previous CHIANTI version. For the $n = 2, 3$ (lowest 46 levels) we adopted the A-values from the MBPT calculations of Wang et al. (2015).

3.15. Ti XIX

The present model for Ti XIX is a significant improvement over the previous one, which only had the 10 lowest $n = 2$ levels and DW collision rates. We retained the 166 bound levels up to $n = 5$ of the Fernández-Mencher et al. (2014a) data. For the $n = 2, 3$ (lowest 46 levels) we adopted the A-values from the MBPT calculations of Wang et al. (2015). Experimental energies are taken from NIST, however we note that several values seem uncertain, and some are estimated energies, i.e. not relative to the ground state.

3.16. Cr XXI

As for Ti XIX, the previous model only had the 10 lowest $n = 2$ levels and DW CE rates. We retained the 166 bound levels up to $n = 5$ of the Fernández-Mencher et al. (2014a) data. For the $n = 2, 3$ (lowest 46 levels) we adopted the A-values from the MBPT calculations of Wang et al. (2015). Experimental energies are taken from NIST. As for Ti XIX, several NIST values seem uncertain, and some are estimated energies, i.e. not relative to the ground state.

3.17. Mn XXII

Also for Mn XXII, the previous model only had the 10 lowest $n = 2$ levels and DW CE rates. We retained the 166 bound levels up to $n = 5$ of the Fernández-Mencher et al. (2014a) data. For the $n = 2, 3$ (lowest 46 levels) we adopted the A-values from the MBPT calculations of Wang et al. (2015). Experimental energies are taken from NIST, but we note that

in several cases observed energies are approximate, as they are not given relative to the ground state.

3.18. *Fe* XXIII

Fe XXIII is an important ion to study solar flares. The previous *Fe* XXIII model had *R*-matrix CE rates for the levels up to $n = 4$, and DW rates for several $n = 5$ levels. In addition, the model had autoionizing levels. We retained the 166 bound levels up to $n = 5$ of the [Fernández-Menchero et al. \(2014a\)](#) data. For the $n = 2, 3$ (lowest 46 levels) we adopted the A-values from the MBPT calculations of [Wang et al. \(2015\)](#). We note that the previous CHIANTI v.9 model had observed energies from NIST. However, as several energies are far from the theoretical values, the CHIANTI v.8 experimental energies have been reinstated, with few additional energies taken from NIST. The data related to the autoionizing levels (producing the satellite lines) are the same as in version 9.

3.19. *Co* XXIV

As for *Ti* XIX, the previous CHIANTI model for *Co* XXIV only had the 10 lowest $n = 2$ levels and DW CE rates. We retained the 166 bound levels up to $n = 5$ of the [Fernández-Menchero et al. \(2014a\)](#) data. For the $n = 2, 3$ (lowest 46 levels) we adopted the A-values from the MBPT calculations of [Wang et al. \(2015\)](#). Experimental energies are taken from NIST, but we note that in several cases, observed energies are approximate, as they are not given relative to the ground state.

3.20. *Ni* XXV

The previous model for *Ni* XXV was relatively accurate, as it had *R*-matrix collisional rates for the lower levels, and DW rates for 92 levels up to $n = 5$. We retained the 166 bound levels up to $n = 5$ of the [Fernández-Menchero et al. \(2014a\)](#) data. For the $n = 2, 3$ (lowest 46 levels) we adopted the A-values from the MBPT calculations of [Wang et al. \(2015\)](#). Experimental energies are mostly taken from the compilation in the previous CHIANTI version, as it takes into account accurate measurements not included in the NIST compilation. We note that many differences are present between the NIST and CHIANTI energies.

3.21. *Zn* XXVII

As for *Ti* XIX, the previous CHIANTI model for *Zn* XXVII only had the 10 lowest $n = 2$ levels and DW collision rates. We retained the 166 bound levels up to $n = 5$ of the [Fernández-Menchero et al. \(2014a\)](#) data. For the $n = 2, 3$ (lowest 46 levels) we adopted the A-values from the MBPT calculations of [Wang et al. \(2015\)](#). Experimental energies are taken from NIST.

4. NEW ATOMIC DATA FOR THE CARBON ISOELECTRONIC SEQUENCE

The CE rates for all the ions in the C-like sequence (from *N* II to *Kr* XXXI), have recently been calculated by [Mao et al. \(2020\)](#) within the UK APAP network with the Breit-Pauli *R*-matrix suite of codes and the intermediate coupling frame transformation (ICFT) method. They included in the configuration interaction (CI) target and close-coupling (CC) collision expansion 590 fine-structure levels, arising from 24 configurations with $n \leq 4$ and the three configurations $2s^2 2p5l$ with $l=0-2$.

The levels above the ionization threshold have not been included, as proper treatment would require an extended two-ion model, which is left for future updates. The A-values of the transitions among the ground configuration $2s^2 2p^2$ and the first excited $2s 2p^3$ levels have been taken from the MCHF calculations of [Tachiev & Froese Fischer \(2001\)](#) and the associated [Tachiev \(2004\)](#) as available online. Duplicates in the data were removed, and multipolar transition probabilities added.

Complete large-scale calculations of electron-impact excitation with the *R*-matrix codes for C-like ions were available in the previous CHIANTI version only for a few ions: *Ne*, *S*, and *Fe*. For most of the ions, *R*-matrix data were only available for the ground configuration $2s^2 2p^2$ levels, with DW CE rates available for the excited configurations.

Ions from the C-like sequence provide widely-used density diagnostics (see, e.g. the review by [Del Zanna & Mason 2018](#)) thanks to the metastability of the ground configuration levels. When benchmarking the new atomic rates, we found for many ions only relatively minor changes (about 20%) in the intensities of the strongest transitions. One exception is *Ar* XIII, because of an increase of about a factor of two in the CE rates for the forbidden transitions within the ground configuration, as shown in [Mao et al. \(2020\)](#). This affects the density diagnostics.

The reason why for most other C-like ions changes are not large is related to the fact that the populations of the ground configuration levels are strongly affected not only by the CE rates within them, but also by cascading from higher levels. In turn, the higher levels are mainly populated by direct impact excitation from the ground state via dipole-allowed transitions. As is well-known (but also shown in [Mao et al. 2020](#)) that the DW CE rates are often close to the *R*-matrix ones for the strongest allowed transitions, the result is that the populations of the ground configuration levels with the new models are not very different, despite some differences being present between the new and previous *R*-matrix CE rates within the ground configuration.

For *N* II we have maintained the previous CHIANTI model as the CE rates are deemed more accurate.

4.1. *O* III

For O III we have retained the 177 bound levels of the Mao et al. (2020) calculations. Regarding the CE rates, as pointed out by Mao et al. (2020) and Morisset et al. (2020), those obtained with the ICFT calculations for the transitions among the ground configuration states differ from the more accurate values such as those calculated by Storey et al. (2014) and Tayal & Zatsarinny (2017) at the low temperatures typical of photoionized plasma. Tayal & Zatsarinny (2017) carried out a B-spline *R*-matrix calculation, but did not provide rates at sufficiently high temperatures needed for, e.g., solar plasma. Storey et al. (2014) performed a set of extended Breit-Pauli *R*-matrix calculations for transitions within the ground configuration, but only provided rates up to 25000 K. We have adopted these latter rates, and used the Mao et al. (2020) ones for the higher temperatures. For some transitions, the Mao et al. (2020) values at 25000 K are only 5–10% higher than the Storey et al. (2014) rates, this difference being comparable with the typical uncertainty of these calculations, as discussed by Storey et al. (2014). Regarding the transition probabilities, we replaced the Mao et al. (2020) A-values for the transitions among the ground configuration $2s^2 2p^2$ and the first excited $2s 2p^3$ levels with the MCHF values. For the observed energies we used the NIST values, but note that several are uncertain, as they were not measured relative to the ground state. The previous CHIANTI model had 46 levels, and a mixture of *R*-matrix and DW data for the CE rates.

4.2. *Ne v – Ca xv*

For Ne v, the new model replaces one with 49 levels and *R*-matrix CE rates. We have retained 304 bound levels, and used the MCHF values as in O III. In this case, nearly all the NIST experimental energies are in good agreement with the theoretical ones.

The new model for Na VI is a significant improvement, as it replaces one with only 20 levels and DW CE rates (except for the ground configuration). We have retained 410 bound levels, and used the MCHF A-values for the transitions among the ground configuration $2s^2 2p^2$ and the first excited $2s 2p^3$ levels.

The previous model for Mg VII had a mixture of scaled *R*-matrix data for the ground configuration, and DW rates for a total of 46 states. We have retained 450 bound levels, and used the MCHF A-values for the transitions among the ground configuration $2s^2 2p^2$ and the first excited $2s 2p^3$ levels.

For Al VIII, the present model is a significant improvement over the previous one, which only had 20 levels and DW CE rates. We have retained 482 bound levels, and used the MCHF A-values for the transitions among the ground configuration $2s^2 2p^2$ and the first excited $2s 2p^3$ levels. Several NIST energies were uncertain and were not included. A few

experimental energies for the ground configuration were improved.

The previous model for Si IX had 46 levels, and a mixture of *R*-matrix data for the ground configuration, and DW rates for the other states. We have retained all 590 levels, and used the MCHF A-values for the transitions among the ground configuration $2s^2 2p^2$ and the first excited $2s 2p^3$ levels.

The new model for P X is a significant improvement, as the previous model had only 20 levels and DW CE rates. We have retained all 590 levels, and used the MCHF ab-initio A-values calculated by G. Tachiev (2004) for the transitions among the ground configuration $2s^2 2p^2$ and the first excited $2s 2p^3$ levels. Several NIST energies were uncertain.

The previous model for S XI was relatively extended, with 74 levels, and a mixture of *R*-matrix data for the ground configuration, and DW rates for the other states. For several levels we have improved the experimental energies over the NIST values. We have retained all 590 levels, and used the MCHF ab-initio A-values calculated by G. Tachiev (2004) for the transitions among the ground configuration $2s^2 2p^2$ and the first excited $2s 2p^3$ levels.

The new model for Cl XII is a significant improvement, as the previous model had only 20 levels and DW CE rates. We have retained all 590 levels, and used the MCHF ab-initio A-values calculated by G. Tachiev (2004) for the transitions among the ground configuration $2s^2 2p^2$ and the first excited $2s 2p^3$ levels.

For Ar XIII, the new model produces line emissivities significantly different than the previous one, which was limited, as it had only 15 levels and DW CE rates. A comparison with version 9 for some important lines was shown in Mao et al. (2020). For version 10, we have retained all 590 levels, and used the MCHF ab-initio A-values calculated by G. Tachiev (2004) for the transitions among the ground configuration $2s^2 2p^2$ and the first excited $2s 2p^3$ levels. Experimental energies are from NIST, but we note that in many instances they are only approximate.

The new model for K XIV is also a significant improvement over the previous one, which had 20 levels and DW CE rates. For version 10, we have retained all 590 levels, and used the MCHF ab-initio A-values calculated by G. Tachiev (2004) for the transitions among the ground configuration $2s^2 2p^2$ and the first excited $2s 2p^3$ levels. The few available experimental energies are from NIST.

For Ca XV, we have retained all 590 levels, and used the MCHF ab-initio A-values calculated by G. Tachiev (2004) for the transitions among the ground configuration $2s^2 2p^2$ and the first excited $2s 2p^3$ levels. For these 15 states, the previous CHIANTI model had *R*-matrix CE rates, while for the remaining 31 levels only DW data were available. The few available experimental energies are from NIST.

4.3. $Ti\text{ XVII} - Zn\text{ XXV}$

The new models for $Ti\text{ XVII}$, $Cr\text{ XIX}$, $Mn\text{ XX}$, $Co\text{ XXII}$, $Ni\text{ XXIII}$, $Zn\text{ XXV}$ are a significant improvement over the previous ones, which had 20 levels and DW CE rates. For version 10, we have retained all 590 levels. The few available experimental energies are from NIST, with the exception of $Zn\text{ XXV}$, for which we adopted the recommended values for the lowest 20 states by Edlen, and one level of $Ni\text{ XXIII}$.

We note that [Ekman et al. \(2014\)](#) calculated accurate energies and A-values with GRASP2K for the C-like ions from $Ar\text{ XIII}$ to $Zn\text{ XXV}$. If users are interested in identifying new experimental energies, the GRASP2K values should be considered. We have not included the A-values from [Ekman et al. \(2014\)](#) as they only provided E1 transitions, and also because the AS energies for these highly charged ions are close to the experimental ones and the A-values are relatively accurate.

4.4. $Fe\text{ XXI}$

$Fe\text{ XXI}$ is an important ion in the sequence. The previous CHIANTI model had an extended set of CE rates calculated with the R -matrix codes by [Badnell & Griffin \(2001\)](#). As shown by [Fernández-Mencher et al. \(2016\)](#), that calculation was somewhat limited in the close-coupling expansion. The [Fernández-Mencher et al. \(2016\)](#) calculations included the same set of configurations in the CI expansion as in [Mao et al. \(2020\)](#), but differed in some details. A few issues were found by [Mao et al. \(2020\)](#) in the [Fernández-Mencher et al. \(2016\)](#) data, so we have replaced the previous model for the bound levels with the CE from [Mao et al.](#)

We have retained the experimental energies as in version 9. We have kept the [Mao et al.](#) A-values, as theoretical energies are quite close to the experimental ones. Very little differences with the previous set of A-values is present. Very small differences of a few percent are found for most of the strongest transitions, between the previous and the new model. The data for the autoionizing levels are the same as in the previous version.

5. NEW ATOMIC DATA FOR THE MG ISOELECTRONIC SEQUENCE

Spectral lines from the Mg-like sequence are useful for a wide range of diagnostics (see, e.g. the review by [Del Zanna & Mason 2018](#)). Among the most important ions in the sequence for solar physics are $Fe\text{ XV}$ and $Si\text{ III}$. For a discussion on $Si\text{ III}$ see [Del Zanna et al. \(2015\)](#).

For this sequence, we have adopted the collisional rates calculated by [Fernández-Mencher et al. \(2014b\)](#) with the ICFT R -matrix codes for all the ions from Al^+ to Zn^{18+} . The target includes a total of 283 fine-structure levels in both the CI target and CC collision expansions, from the con-

figurations $1s^2 2s^2 p^6 3\{s, p, d\} nl$ with $n = 4, 5$, and $l = 0 - 4$. The levels above the ionization threshold have not been included, as proper treatment would require an extended two-ion model, which is left for future updates.

As in the case of the Be-like sequence, previous CHIANTI versions did not have atomic rates for many minor ions, and for the less important ones only had a very limited set of levels and DW CE rates. As shown in [Fernández-Mencher et al. \(2014b\)](#), significant differences with the DW rates are present.

For the radiative rates, we have mostly used the values from the MCHF calculations by [Tachiev & Froese Fischer \(2002\)](#) for the lowest 26 $n = 3$ levels ($3s^2, 3s3p, 3p^2, 3s3d, 3p3d$). Duplicates in the data were removed, and multipolar transition probabilities added. Differences with the [Fernández-Mencher et al. \(2014b\)](#) values were typically at most 20-30%.

5.1. $Al\text{ II}$

The previous CHIANTI model had 20 levels and CE rates obtained from various sources. We have retained the lowest 60 bound states of the [Fernández-Mencher et al.](#) model. Experimental energies are taken from NIST, but we note that a few are uncertain. The original radiative data in [Fernández-Mencher et al. \(2014b\)](#) have been retained for consistency, as significant differences with the MCHF calculations for the higher levels are present.

5.2. $Si\text{ III}$

The previous CHIANTI model had 20 levels and R -matrix CE rates. We have retained the lowest 82 bound states of the [Fernández-Mencher et al.](#) model. Experimental energies are taken from [Del Zanna et al. \(2015\)](#) and NIST.

5.3. PIV

This is a new addition to the database. We have retained the lowest 117 bound states of the [Fernández-Mencher et al.](#) model. Experimental energies are taken from NIST.

5.4. $S\text{ V}$

The previous CHIANTI model was very limited, as it had only 16 levels and DW CE rates calculated in LS coupling. We have retained the lowest 159 bound states of the [Fernández-Mencher et al.](#) model. Significant differences with the previous CE rates are present, as pointed out in [Fernández-Mencher et al.](#) Experimental energies are taken from NIST.

5.5. $Cl\text{ VI}$

This is a new addition to the database. We have retained the lowest 171 bound states of the [Fernández-Mencher et al.](#) model. Experimental energies are taken from NIST.

5.6. *Ar* VII

The previous CHIANTI model was very limited, as it had only 16 levels and DW CE rates calculated in *LS* coupling. We have retained the lowest 196 bound states of the Fernández-Menchero et al. model. Experimental energies are taken from NIST.

5.7. *K* VIII

This is a new ion for the database. We have retained the lowest 209 bound states of the Fernández-Menchero et al. model. Experimental energies are taken from NIST.

5.8. *Ca* IX

The previous CHIANTI model was extended, with the complete set of 283 levels up to $n = 5$, but DW CE rates. Autoionising levels were also present. We have retained the lowest 220 bound states of the Fernández-Menchero et al. model. Experimental energies are taken from the previous CHIANTI version.

5.9. *Ti* XI

The previous CHIANTI model had only 16 levels and interpolated CE rates. For this ion and the following ones, we have retained all 283 levels from Fernández-Menchero et al. (2014b) as they are all bound states. Experimental energies are taken from NIST.

5.10. *Cr* XIII

The previous CHIANTI model had only 16 levels and DW CE rates calculated in *LS* coupling. Experimental energies are taken from NIST.

5.11. *Mn* XIV

Mn XIV is a new addition to the database. Experimental energies are taken from NIST.

5.12. *Fe* XV

The previous CHIANTI model was extended, with the complete set of 283 levels up to $n = 5$, and *R*-matrix CE rates for the $n = 3$ levels, and DW CE rates for the higher levels. The experimental energies of the previous version 9 are retained. As mentioned in Fernández-Menchero et al. (2014b), significant differences with the previous *R*-matrix CE rates are present in some cases, for this important ion. As a follow-up, Fernández-Menchero et al. (2015b) discussed in more detail some *Fe* XV transitions, and presented a benchmark against solar data.

5.13. *Co* XVI

Co XVI is a new addition to the database. Experimental energies are taken from NIST.

5.14. *Ni* XVII

The previous CHIANTI model was relatively extended, with the complete set of 159 levels up to $n = 5$, but DW CE rates. Observed energies are taken from a variety of sources, as detailed in the database.

5.15. *Zn* XIX

Zn XIX is a new addition to the database. Experimental energies are taken from NIST.

6. OTHER UPDATED IONS

6.1. *Fe* XII

Experimental energies of a few $n = 3$ levels in *Fe* XII were changed in version 9 following the work of Wang et al. (2018a), which confirmed most of the identifications by Del Zanna & Mason (2005). However, by mistake the indexing of two levels (37,38) was interchanged, so the energies for these two levels were incorrect. This has been fixed. The energies of a few $4d$ levels have now been changed, following Song et al. (2020). These authors have carried out MCDHF calculations and compared predicted and observed wavelengths for the $n = 4$ levels. Excellent agreement with the wavelengths of the new identifications proposed by Del Zanna (2012) was found. Generally, excellent agreement was also found with the wavelengths and identifications by Fawcett et al. (1972), with the exception of several $4d$ levels. After checking the original plates used by Fawcett et al. (1972), and estimating line intensities based on the Del Zanna et al. (2012a) calculations, Song et al. (2020) recommended a few new values, which have been adopted here.

6.2. *Fe* XI

Wang et al. (2018b) carried out extensive MCDHF calculations for the $n = 3$ levels in *Fe* XI, and compared energies with literature values. For the $3s^23p^33d$ levels, producing the strongest lines, they found excellent agreement (within a few hundreds of Kaysers) with all the new identifications proposed by Del Zanna (2010) and included in previous CHIANTI versions. For the $3s3p^33d$ levels, the four previous tentative identifications proposed by Del Zanna (2010) have been revised following Wang et al. (2018b).

6.3. *Fe* X

Wang et al. (2020) carried out extensive MCDHF calculations for *Fe* X, and assessed the wavelengths and identifications, as present in NIST, the previous CHIANTI versions, and literature values. Good general agreement with the values proposed by Del Zanna et al. (2004) and Del Zanna et al. (2012b), included in previous CHIANTI versions was found, with notable discrepancies in a few NIST energies. On the basis of the Wang et al. (2020) assessment,

we have introduced 8 revised experimental energies, three from [Jupen et al. \(1993\)](#), one from [Del Zanna et al. \(2012b\)](#) and four from NIST.

The energy separation of the $^4D_{7/2}$ and $^4D_{5/2}$ has been modified by using the recent measurement by [Landi et al. \(2020\)](#), decreasing it from the previous 5.5 cm^{-1} value (see the discussion in [Del Zanna et al. 2004](#)) to 2.29 cm^{-1} . This change has negligible effects on the wavelengths of the lines emitted by these levels around 257.26 \AA , but it has a critical importance for the measurement of magnetic field strength using the magnetically induced transition from the $^4D_{7/2}$ level to the ground ([Landi et al. 2020b, in press](#)).

6.4. Ni XII

Regarding Ni XII, we base our new model on the Breit-Pauli R -matrix calculations carried out with the ICFT method by [Del Zanna & Badnell \(2016\)](#). The CI expansion included the complete set of atomic states up to $n = 4$, but for the CC expansions in the scattering calculation only the lowest 312 LS terms were retained. This is a significant improvement over the previous calculations (available in the previous CHI-ANTI version) which included only the lowest 14 terms (up to 3d), producing 31 fine-structure levels. We provide only the lowest 589 fine-structure levels, as the higher ones are not reliable. A key feature of the [Del Zanna & Badnell \(2016\)](#) calculations is the inclusion of semi-empirical corrections in the structure and scattering calculations. This provides a significant improvement in the rates.

Very few energy levels were known for this ion, the most important ones only relative to the 3d $^4D_{7/2}$ (the same situation which occurred in Fe X, resolved by [Del Zanna et al. 2004](#)). [Del Zanna & Badnell \(2016\)](#) provided a discussion of the various optional line identifications, and suggested several new ones. The MCDHF calculations by [Wang et al. \(2020\)](#) were used by the same authors to confirm some of those identifications and suggest new ones. We adopt these latest values in the present model, but point out that further laboratory studies are needed to confirm these identifications.

6.5. Cr VIII

Cr VIII was added to CHIANTI in version 6 ([Dere et al. 2009](#)) using data from an unpublished calculation of E. Landi. This has been replaced with the data from [Aggarwal et al. \(2009\)](#) giving a model with 362 fine structure levels from 10 configurations.

Experimental energies are only available for 21 levels and have been taken from the NIST database. [Aggarwal et al. \(2009\)](#) performed a number of structure calculations, and the theoretical energies used for CHIANTI are those from the GRASP calculation with Breit and QED corrections. Radiative data are also from the GRASP calculation. This data-set was filtered such that, for each atomic level, only those decay

rates that were $> 10^{-5}$ of the maximum decay rate from that level were retained.

Upsilon were calculated by [Aggarwal et al. \(2009\)](#) using the Flexible Atomic Code and were tabulated at nine temperatures from $\log T = 5.0$ to 6.6 at 0.2 dex intervals. Cr VIII has 10 metastable levels plus the ground state and only those transitions from these 110 levels were included in the CHI-ANTI data file. The collision dataset was assessed following the procedure described in CHIANTI Technical Report No. 4 and 69 allowed transitions were found not to tend towards their high temperature limits, with the limits generally higher than the upsilon values sometimes by as much as a factor 100. These discrepancies may stem from the different structure models used for the radiative and collisional calculations. For these 69 transitions, the high temperature limits were removed from the fits. The final CHIANTI scaled-upsilon file reproduces the original upsilon data to better than 0.2%.

6.6. Fe VII

Fe VII has not been updated since CHIANTI 5 ([Landi et al. 2006](#)), and the model contained only the nine levels of the ground configuration. The new model has 189 fine-structure levels of the $3p^63d^2$, $3p^53d^3$, $3p^53d4l$ ($l = s, p, d, f$) and $3p^53d5l$ ($l = s, p$) configurations. The model was not previously updated because inconsistencies between line intensities calculated with the [Witthoeft & Badnell \(2008\)](#) model and solar observations (using the NIST identifications) were noted, but different explanations were given: [Young & Landi \(2009\)](#) revised some NIST identifications but assumed that the inconsistencies were due to problems in the atomic rates. [Del Zanna \(2009\)](#) provided an alternative set of identifications where agreement with observations was obtained, pointing out that the [Witthoeft & Badnell \(2008\)](#) model was relatively correct, by comparison with a large-scale benchmark calculation. Later, [Tayal & Zatsarinsky \(2014\)](#) provided a new large-scale scattering calculation producing similar rates to those of [Witthoeft & Badnell \(2008\)](#).

The new model follows the assessment of [Young et al. \(2020, submitted\)](#), which relies on new laboratory measurements. Some inconsistencies are still present but the new model represent a significant improvement over the previous one. The experimental energies are mostly taken from the NIST database, but some new values are taken from [Young et al.](#) and [Young & Landi \(2009\)](#). Theoretical energies for 134 levels are taken from [Li et al. \(2018\)](#), while the remaining energies are from [Tayal & Zatsarinsky \(2014\)](#). We note that the [Li et al. \(2018\)](#) energies show much better agreement with the experimental energies than those of [Tayal & Zatsarinsky \(2014\)](#), and so they yield more accurate wavelengths for transitions involving levels without experimental energies.

Radiative decay rates for allowed transitions are from Tayal & Zatsariny (2014). Forbidden transition data are from Li et al. (2018), supplemented with values from Witthoeft & Badnell (2008), where necessary.

Collisional excitation rates are from Tayal & Zatsariny (2014). The CHIANTI assessment procedure identified a number of allowed transitions for which the rates did not tend towards the high temperature limit points, usually with the latter being too high. These cases likely arise because the decay rates were derived from a more elaborate structure calculation than used for the scattering calculation. They were treated by adjusting the upsilon scaling parameter to enable a smooth transition to the high temperature limit.

6.7. O II

It was brought to our attention that four A-values within the ground configuration of the N-like O II were incorrectly assigned. We have now replaced them with the correct ones, noting that this error only affected the intensities of some of the forbidden lines within the ground configuration. We have also improved the experimental energies and associated wavelengths using literature values.

7. NEW ADDITIONS TO THE DATABASE

7.1. Cr II

The vanadium-like ion Cr II has been added to CHIANTI. Tayal & Zatsariny (2020) provided radiative decay rates and Maxwellian-averaged collision strengths (upsilons) for 512 fine structure levels of the $3d^5$, $3d^45s$, $3d^44p$, $3d^34s^2$ and $3d^34s4p$ configurations. Experimental energies were available for 378 levels and were taken from the NIST database. We note that the agreement between the experimental energies and the Tayal & Zatsariny (2020) calculated energies is excellent, with a mean discrepancy of 38 cm^{-1} . The radiative decay rate data-set was filtered such that, for each atomic level, only those decay rates that were $> 10^{-5}$ of the maximum decay rate from that level were retained.

Based on the radiative data we determined that there are 117 metastable levels (including the ground) and so the upsilon data-set was filtered so that only those transitions for which the lower level was a metastable were included. Upsilons were tabulated for 20 temperatures between 10^3 and 10^5 K. The assessment method described in CHIANTI Technical Report No. 4 was applied to the data-set and no problem transitions were found. The scaled upsilon data stored in CHIANTI reproduce the original data to better than 0.5% for all transitions and temperatures.

8. POPULATION LOOKUP TABLES

IDL software has been written to generate lookup tables for level populations for all ions in the database. The CHIANTI software can then use these tables to obtain level populations

rather than compute them from the atomic data. This has significant time savings for the large ion models in CHIANTI. For example, a synthetic spectrum that would usually take about 10 minutes to compute can be obtained in less than a minute with the lookup tables. We are also experimenting other ways to speed-up the calculations. Details will be made available within the software notes.

To create the lookup tables, the software scales the level populations by one of two formulae, depending if the level is a metastable or not:

$$n'_i = \begin{cases} 10^{5+\alpha_i/T} n_i & [\text{regular}] \\ 10^{20+\alpha_i/T} \frac{n_i}{N_e} & [\text{metastable}] \end{cases} \quad (1)$$

where T is temperature, N_e is the electron number density, n_i the level population computed by the IDL routine `pop_solver`, and α_i a scaling parameter described below. The n'_i are computed for a temperature range T_0 to T_1 determined from the default ionization equilibrium file distributed with CHIANTI to be those temperatures for which the ionization fraction values are $\geq 10^{-8}$ of the peak value. The density range is set by the user. The temperature and density grids are set on a logarithmic scale with intervals of 0.05 and 0.2 dex, respectively.

The advantage of tabulating the level populations rather than, say, the emissivities or contribution functions is that the data-set is much smaller. For example, the density range $\log N_e = 7$ to 13 yields tables with a total size of about 0.5 Gbytes.

The temperature dependence of a level population is usually given by $\exp(-1/T)$, hence the temperature factor in Eq. 1. The parameter α is determined from the following expression:

$$\alpha = \frac{T_0 T_1}{T_1 - T_0} (\log \bar{n}(T_1) - \log \bar{n}(T_0)) \quad (2)$$

where $\bar{n}(T)$ is the mean value of the level population over the density range of the lookup table.

The scaling applied to the level populations is chosen to remove the dominant temperature and density dependent terms from the tabulated quantity. When deriving populations from the lookup tables bilinear interpolation is used, and the accuracy of the derived populations is typically better than 1%. Further details of the method are given in CHIANTI Technical Report No. 16.

A set of lookup tables is provided for *Solarsoft* users in the CHIANTI package, computed over the density range $\log N_e = 7$ to 13. For other users tables for all ions can be generated with the routine `ch_lookup_all_ions`.

A `/lookup` keyword has been added to key IDL routines such as `dens_plotter`, `temp_plotter` and `ch_synthetic` to implement the lookup tables. In addition the new routines `ch_lookup_emiss` and

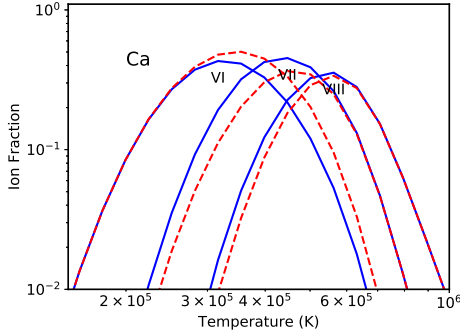


Figure 5. A comparison of the new ionization equilibrium (blue line) to that of version 9 (red dashed line) for several stages of calcium

`ch_lookup_gofnt` yield emissivities and contribution functions from the lookup tables. A key feature of the software is that the CHIANTI version number is checked to ensure the lookup tables come from the latest version of the database.

9. IMPROVED RECOMBINATION RATES AND IONIZATION EQUILIBRIA

New calculations of the radiative and dielectronic recombination rates for silicon-like ions recombining to phosphorus-like ions have been presented by [Kaur et al. \(2018\)](#). These have been incorporated into CHIANTI together with a new calculation of the ionization equilibrium. They do not represent large changes in the ionization equilibrium. For the case of calcium, the changes between the Version 9 and the new Version 10 ionization can be seen in Fig. 5.

10. DIELECTRONIC RECOMBINATION (DR)

10.1. Dielectronic recombination into helium-like ions

Recently, a large-scale collisional-radiative model for helium emission in the solar corona was developed ([Del Zanna et al. 2020](#)). Whilst benchmarking the various atomic rates, some inconsistencies in the current CHIANTI model for neutral helium were found. However, the present model has not been modified as it is very limited in terms of physical processes included. The main error that was found was in the dielectronic recombination (DR) into neutral helium, as calculated by N.R.Badnell. New DR rates were recalculated by [Del Zanna et al. \(2020\)](#). The new rates are about a factor of two higher and have now been included in CHIANTI. The error was also present (albeit not as large) for the corresponding Li, Be, and B ions, which have also been updated in the UK APAP repository and in the present CHIANTI version.

10.2. Suppression of dielectronic recombination rates

CHIANTI uses total DR rate coefficients in the calculation of the equilibrium ionization balance, and the so-called

"zero-density" rates are used, meaning there is no density sensitivity. It is known, however, that DR rates become suppressed at high densities as the increased electron collision rates de-populate the high-lying levels that are important in the DR process. [Summers \(1974\)](#) modeled this process, and [Nikolić et al. \(2018\)](#) provided a fitting formula that is applicable to all ions in the CHIANTI database. With CHIANTI 10 we have coded the [Nikolić et al. \(2018\)](#) suppression factor formula and the IDL routine `ch_dr_suppress` returns the DR rate coefficient for any ion for a specified electron number density (N_e) or electron pressure (P). If the latter is specified, then the density is set to P/T , where T is the temperature.

A consequence of the DR rates is that the equilibrium ionization balance table (stored in a CHIANTI "ioneq" file) becomes density dependent. The IDL routine `make_ioneq_all` generates the ioneq file and it now takes the optional inputs "density" and "pressure". The default CHIANTI ioneq file that is distributed with the database (named "chianti.ioneq") continues to be the zero-density table.

We caution that the suppression factor formula is an approximation and that there are other sources of density sensitivity to the ionization equilibrium equations that are not modeled. In particular that due to ionization/recombination out of metastable levels, as recently discussed for carbon and oxygen ions by [Dufresne & Del Zanna \(2019\)](#) and [Dufresne et al. \(2020\)](#).

Further details are given in CHIANTI Technical Report No. 17, and examples of the use of the new ioneq files are given in [Young et al. \(2018\)](#) and [Young \(2018\)](#).

11. CONCLUSIONS

As described in a recent review on the status of the atomic data and modelling available within CHIANTI ([Del Zanna & Young 2020](#)), the present version is a significant step forward in terms of completeness of atomic data for astrophysical ions. Significant improvements are provided for several ions for which little or no data were available. The most important improvements are for the ions of the Be-like sequence, as we have shown with one example. For those cases where accurate atomic data were available in the previous version, the recent large-scale calculations (scattering and radiative) often produce line emissivities for the strongest lines that are reasonably close (within 10-20%) to those obtained from the previous data, providing confidence in the atomic data and also a measure on the overall uncertainties. As briefly mentioned here and also pointed out in [Del Zanna & Young \(2020\)](#), several improvements on the modelling side are however still required, with also the inclusion of more physical processes such as photoionization,

charge exchange, collisional ionization from excited states, etc.

ACKNOWLEDGMENTS

GDZ acknowledges support from STFC (UK) via the consolidated grants to the atomic astrophysics group (AAG) at DAMTP, University of Cambridge (ST/P000665/1. and ST/T000481/1). PRY and KPD acknowledge support from the NASA Heliophysics Data Environment Enhancements program. The UK APAP network calculations have been funded by STFC via the University of Strathclyde (grants No. PP/E001254/1 and ST/J000892/1., and ST/R000743/1).

We would like to thank all our colleagues who provided data in electronic format or pointed out issues

with the database. In particular, we thank Kai Wang, Christophe Morisset, John Raymond, Claudio Mendoza, Roger Dufresne, Nigel Badnell and Peter Storey. EL acknowledges support from NSF grants AGS 1408789, 1460170, and NASA grants NNX16AH01G, NNX17AD37G and 80NSSC18K0645.

REFERENCES

Aggarwal, K. M., Kato, T., Keenan, F. P., & Murakami, I. 2009, *A&A*, 506, 1501

Aggarwal, K. M., & Keenan, F. P. 2012, *PhyS*, 85, 065301

—. 2015, *MNRAS*, 447, 3849

Aggarwal, K. M., Keenan, F. P., & Lawson, K. D. 2016, *MNRAS*, 461, 3997

Anderson, M., Appourchaux, T., Auchère, F., et al. 2019, *A&A*, doi:<https://doi.org/10.1051/0004-6361/201935574>

Badnell, N. R. 2011, *Computer Physics Communications*, 182, 1528

Badnell, N. R., Del Zanna, G., Fernández-Menchero, L., et al. 2016, *Journal of Physics B Atomic Molecular Physics*, 49, 094001

Badnell, N. R., & Griffin, D. C. 2001, *Journal of Physics B Atomic Molecular Physics*, 34, 681

Beiersdorfer, P., Bitter, M., von Goeler, S., & Hill, K. W. 1989, *PhRvA*, 40, 150

Briand, J. P., Tavernier, M., Marrus, R., & Desclaux, J. P. 1984, *PhRvA*, 29, 3143

Chantler, C. T., Payne, A. T., Gillaspy, J. D., et al. 2014, *New Journal of Physics*, 16, 123037

Chidichimo, M. C., Del Zanna, G., Mason, H. E., & et al. 2005, *A&A*, 430, 331

Del Zanna, G. 1999, PhD thesis, University of Central Lancashire, UK

Del Zanna, G. 2009, *A&A*, 508, 501

—. 2010, *A&A*, 514, A41+

—. 2012, *A&A*, 546, A97

—. 2019, *A&A*, 624, A36

Del Zanna, G., & Badnell, N. R. 2016, *A&A*, 585, A118

Del Zanna, G., Berrington, K. A., & Mason, H. E. 2004, *A&A*, 422, 731

Del Zanna, G., Bromage, B. J. I., Landi, E., & Landini, M. 2001, *A&A*, 379, 708

Del Zanna, G., Fernández-Menchero, L., & Badnell, N. R. 2015, *A&A*, 574, A99

Del Zanna, G., Fernández-Menchero, L., & Badnell, N. R. 2019, *MNRAS*, 484, 4754

Del Zanna, G., & Mason, H. E. 2005, *A&A*, 433, 731

—. 2018, *Living Reviews in Solar Physics*, 15

Del Zanna, G., Rozum, I., & Badnell, N. 2008, *A&A*, 487, 1203

Del Zanna, G., Storey, P. J., Badnell, N. R., & Andretta, V. 2020, *ApJ*, 898, 72

Del Zanna, G., Storey, P. J., Badnell, N. R., & Mason, H. E. 2012a, *A&A*, 543, A139

—. 2012b, *A&A*, 541, A90

Del Zanna, G., & Young, P. R. 2020, *Atoms*, 8, 46

Dere, K. P., Del Zanna, G., Young, P. R., Landi, E., & Sutherland, R. S. 2019a, *ApJS*, 241, 22

—. 2019b, *ApJS*, 241, 22

Dere, K. P., Landi, E., Young, P. R., & Del Zanna, G. 2001, *ApJS*, 134, 331

Dere, K. P., Landi, E., Young, P. R., et al. 2009, *A&A*, 498, 915

Derevianko, A., & Johnson, W. R. 1997, *PhRvA*, 56, 1288

Dubau, J., Loulorgue, M., Gabriel, A. H., Steenman-Clark, L., & Volonte, S. 1981, *MNRAS*, 195, 705

Dufresne, R. P., & Del Zanna, G. 2019, *A&A*, 626, A123

Dufresne, R. P., Del Zanna, G., & Badnell, N. R. 2020, *MNRAS*, 497, 1443

Dyall, K. G., Grant, I. P., Johnson, C. T., Parpia, F. A., & Plummer, E. P. 1989, *Comput. Phys. Commun.*, 55, 425

Ekman, J., Jönsson, P., Gustafsson, S., et al. 2014, *A&A*, 564, A24

Fawcett, B. C., & Hayes, R. W. 1987, *PhyS*, 36, 80

Fawcett, B. C., Kononov, E. Y., Hayes, R. W., & Cowan, R. D. 1972, *Journal of Physics B Atomic Molecular Physics*, 5, 1255

Fernández-Menchero, L., Del Zanna, G., & Badnell, N. R. 2014a, *A&A*, 566, A104

—. 2014b, *A&A*, 572, A115

—. 2015a, *MNRAS*, 450, 4174

—. 2015b, *A&A*, 577, A95

Fernández-Menchero, L., Giunta, A. S., Del Zanna, G., & Badnell, N. R. 2016, *Journal of Physics B Atomic Molecular Physics*, 49, 085203

Fernández-Menchero, L., Zatsarinny, O., & Bartschat, K. 2017, *Journal of Physics B Atomic Molecular Physics*, 50, 065203

Froese Fischer, C., Godefroid, M., Brage, T., Jönsson, P., & Gaigalas, G. 2016, *Journal of Physics B Atomic Molecular Physics*, 49, 182004

Gabriel, A. H. 1972, *MNRAS*, 160, 99

Gabriel, A. H., & Jordan, C. 1969, *MNRAS*, 145, 241

Goryaev, F. F., Vainshtein, L. A., & Urnov, A. M. 2017, *Atomic Data and Nuclear Data Tables*, 113, 117

Grant, I. P., McKenzie, B. J., Norrington, P. H., Mayers, D. F., & Pyper, N. C. 1980, *Comput. Phys. Commun.*, 21, 207

Gu, M. F. 2008, *Canadian Journal of Physics*, 86, 675

Indelicato, P. 2019, *Journal of Physics B Atomic Molecular Physics*, 52, 232001

Jönsson, P., Gaigalas, G., Bierón, J., Fischer, C. F., & Grant, I. P. 2013, *Computer Physics Communications*, 184, 2197

Jönsson, P., He, X., Froese Fischer, C., & Grant, I. P. 2007, *Comput. Phys. Commun.*, 177, 597

Jönsson, P., Gaigalas, G., Rynkun, P., et al. 2017, *Atoms*, 5, 16

Jupen, C., Isler, R. C., & Trabert, E. 1993, *MNRAS*, 264, 627

Kato, T., Safranova, U., Shlypteseva, A., et al. 1997, *Atomic Data and Nuclear Data Tables*, 67, 225

Kaur, J., Gorczyca, T. W., & Badnell, N. R. 2018, *A&A*, 610, A41

Keenan, F. P., Berrington, K. A., Burke, P. G., Dufton, P. L., & Kingston, A. E. 1986, *PhyS*, 34, 216

Kelly, R. L. 1987, *Journal of Physical and Chemical Reference Data*, 17

Khardi, S., Buchet-Poulizac, M. C., Buchet, J. P., et al. 1994, *PhyS*, 49, 571

Kramida, A., Yu. Ralchenko, Reader, J., & and NIST ASD Team. 2015, *NIST Atomic Spectra Database* (ver. 5.3), [Online]. Available: <http://physics.nist.gov/asd> [2017, August 23]. National Institute of Standards and Technology, Gaithersburg, MD.,

Kramida, A. E., & Träbert, E. 1995, *PhyS*, 51, 209

Kubiček, K., Mokler, P. H., Mäckel, V., Ullrich, J., & López-Urrutia, J. R. C. 2014, *PhRvA*, 90, 032508

Landi, E., Del Zanna, G., Young, P. R., et al. 2006, *ApJS*, 162, 261

Landi, E., Hutton, R., Brage, T., & Li, W. 2020, *ApJ*, 902, 21

Li, Y., Xu, X., Li, B., Jönsson, P., & Chen, X. 2018, *MNRAS*, 479, 1260

Machado, J., Szabo, C. I., Santos, J. P., et al. 2018, *PhRvA*, 97, 032517

Malyshev, A. V., Kozhedub, Y. S., Glazov, D. A., Tupitsyn, I. I., & Shabaev, V. M. 2019, *PhRvA*, 99, 010501

Mao, J., Badnell, N. R., & Del Zanna, G. 2020, *A&A*, 634, A7

Martin, W. C., S. J. M. A., & Dalton, G. R. 1995, *NIST Atomic Spectra Database* (ver. 1.0), [Online]. Available: <http://physics.nist.gov/asd> [1995]. National Institute of Standards and Technology, Gaithersburg, MD.,

Morisset, C., Luridiana, V., García-Rojas, J., et al. 2020, *arXiv e-prints*, arXiv:2009.10586

Nikolić, D., Gorczyca, T. W., Korista, K. T., et al. 2018, *ApJS*, 237, 41

Parmar, A. N., Culhane, J. L., Rapley, C. G., et al. 1981, *MNRAS*, 197, 29P

Payne, A. T., Chantler, C. T., Kinnane, M. N., et al. 2014, *Journal of Physics B Atomic Molecular Physics*, 47, 185001

Pike, C. D., Phillips, K. J. H., Lang, J., et al. 1996, *ApJ*, 464, 487

Rice, J. E., Reinke, M. L., Ashbourn, J. M. A., et al. 2014, *Journal of Physics B Atomic Molecular Physics*, 47, 075701

Rudolph, J. K., Bernitt, S., Epp, S. W., et al. 2013, *PhRvL*, 111, 103002

Schleinkofer, L., Bell, F., Betz, H.-D., Trollmann, G., & Rothermel, J. 1982, *Physica Scripta*, 25, 917. <https://doi.org/10.1088%2F0031-8949%2F25%2F6b%2F004>

Si, R., Li, S., Wang, K., et al. 2017, *A&A*, 600, A85

Smith, R. K., Chen, G.-X., Kirby, K., & Brickhouse, N. S. 2009, *ApJ*, 700, 679

Song, C. X., Wang, K., Del Zanna, G., et al. 2020, *ApJS*, 247, 70

Storey, P. J., Sochi, T., & Badnell, N. R. 2014, *MNRAS*, 441, 3028

Summers, H. P. 1974, *MNRAS*, 169, 663

Tachiev, G., & Froese Fischer, C. 1999, *Journal of Physics B Atomic Molecular Physics*, 32, 5805

—. 2001, *Canadian Journal of Physics*, 79, 955

—. 2002, <https://nle.nist.gov/MCHF/periodic.html>

Tanaka, K., Watanabe, T., Nishi, K., & Akita, K. 1982, *ApJL*, 254, L59

Tayal, S. S., & Zatsarinny, O. 2014, *ApJ*, 788, 24

—. 2017, *ApJ*, 850, 147

—. 2020, *ApJ*, 888, 10

Wang, K., Jönsson, P., Del Zanna, G., et al. 2020, *ApJS*, 246, 1

Wang, K., Jönsson, P., Gaigalas, G., et al. 2018a, *ApJS*, 235, 27

Wang, K., Guo, X. L., Liu, H. T., et al. 2015, *ApJS*, 218, 16

Wang, K., Song, C. X., Jönsson, P., et al. 2018b, *ApJS*, 239, 30

Weller, M. E., Beiersdorfer, P., Lockard, T. E., et al. 2019, *ApJ*, 881, 92

Whiteford, A. D., Badnell, N. R., Ballance, C. P., et al. 2001, *Journal of Physics B Atomic Molecular Physics*, 34, 3179

Wilhelm, K., Curdt, W., Marsch, E., et al. 1995, *SoPh*, 162, 189
Withoeft, M. C., & Badnell, N. R. 2008, *A&A*, 481, 543
Woods, T. N., Eparvier, F. G., Hock, R., et al. 2012, *SoPh*, 275, 115
Young, P. R. 2018, *ApJ*, 855, 15
Young, P. R., Keenan, F. P., Milligan, R. O., & Peter, H. 2018, *ApJ*, 857, 5
Young, P. R., & Landi, E. 2009, *ApJ*, 707, 173